

Satellite-Based Ranking of the World's Hottest and Coldest Cities Reveals Inequitable Distribution of Temperature Extremes

Jiufeng Li, Wenfeng Zhan, T. C. Chakraborty, Zihan Liu, Huilin Du, Weilin Liao, Ming Luo, Long Li, Shiqi Miao, Huyan Fu, Shasha Wang, Fan Huang, and Manchun Li

ABSTRACT: The identification of the world's hottest and coldest cities fascinates both the public and the scientific community. However, the ranking of city temperatures, especially from the perspective of human discomfort, has been difficult. Here we estimated the monthly mean maximum and minimum 1-km resolution urban temperatures of 13,135 cities worldwide (2003–19) from the thermal discomfort perspective by combining in situ measurements, satellite-based land surface temperatures, fine-resolution intracity data, and reanalysis data. Manama, Bahrain, was identified as the hottest city ($48.18^{\circ} \pm 1.31^{\circ}\text{C}$) and Yakutsk, Russia ($-42.96^{\circ} \pm 0.72^{\circ}\text{C}$), as the coldest city. The global city temperatures followed a power-law pattern, characterized by cities with <0.3 million inhabitants covering 80% of the top 20% global cities with extreme temperatures. Our study reveals an inequitable pattern of global city temperature extremes and highlights the urgency of developing appropriate strategies to reduce climate change risks in small- and medium-sized cities with low development levels.

KEYWORDS: Climate change; Temperature; Automatic weather stations; Climate records; Remote sensing; Machine learning

<https://doi.org/10.1175/BAMS-D-22-0233.1>

Corresponding author: Wenfeng Zhan, zhanwenfeng@nju.edu.cn

Supplemental material: <https://doi.org/10.1175/BAMS-D-22-0233.2>

In final form 18 April 2023

©2023 American Meteorological Society

For information regarding reuse of this content and general copyright information, consult the [AMS Copyright Policy](#).

AFFILIATIONS: J. Li, Liu, Du, L. Li, Miao, Wang, and Huang—Jiangsu Provincial Key Laboratory of Geographic Information Science and Technology, International Institute for Earth System Science, Nanjing University, Nanjing, Jiangsu, China; Zhan—Jiangsu Provincial Key Laboratory of Geographic Information Science and Technology, International Institute for Earth System Science, Nanjing University, and Jiangsu Center for Collaborative Innovation in Geographical Information Resource Development and Application, Nanjing, Jiangsu, China; Chakraborty—Atmospheric Sciences and Global Change Division, Pacific Northwest National Laboratory, Richland, Washington; Liao and Luo—Guangdong Key Laboratory for Urbanization and Geo-Simulation, School of Geography and Planning, Sun Yat-sen University, Guangzhou, Guangdong, China; Fu—Department of Geographic Information Science, School of Earth Sciences, Yunnan University, Kunming, Yunnan, China; M. Li—School of Geography and Ocean Science, Nanjing University, Nanjing, Jiangsu, China

Climate change can pose a series of socioeconomic and health impacts on urban residents (World Economic Forum 2019). The hottest and coldest temperatures are two key indicators of climate extremes that have long been the attention of scientists and the public, and on which remarkable progress has been made in recent years (Azarderakhsh et al. 2020; Mildrexler et al. 2011; Y. Zhao et al. 2021). The hottest or coldest temperatures can be determined on two scales: for natural landscapes that include cities and for cities only. Traditionally, the hottest (or coldest) temperatures for natural landscapes have been identified using in situ near-surface air temperature (NSAT) measurements (Turner et al. 2009; El Fadli et al. 2013), and the results have been widely reported by the news media (Amos 2013; Samenow 2016; BBC News 2020; de León and Schwartz 2020; Readfearn 2020). In contrast, relatively fewer studies have focused on the extreme temperatures of global cities due to the lack of appropriate and consistent temperate observations within cities. Currently, most reports of extreme temperature reports in cities are informal (BBC News 2010, 2017; Farmer 2021; Haddad 2021), and a globally consistent framework for ranking cities based on temperature is lacking.

Cities are characterized by strong spatial heterogeneity in temperature (Clemens et al. 2021). However, identifying the world's hottest and coldest cities requires spatially dense temperature observations, which are generally unavailable (Muller et al. 2013). Traditional weather stations, which are often installed outside urban boundaries, are not ideal for determining extreme temperatures inside cities (Zhou et al. 2019). A closer investigation revealed that only 9% of global weather stations are installed over urban surfaces, i.e., one station per 176 km² on average (note S1 the online supplemental material; <https://doi.org/10.1175/BAMS-D-22-0233.2>). For most underdeveloped cities, where urban populations are more vulnerable to climate extremes (Tuholske et al. 2021), usable weather stations are even fewer or entirely absent (Fig. S1). Further analysis revealed that high-income cities only account for 15% of all major cities, but contain approximately 45% of global urban stations (note S1).

Satellite-based observations such as land surface temperature (LST) can provide pixel-by-pixel observations with high spatiotemporal resolution over global cities (Chakraborty and Lee 2019). Satellite-based LST samples the two-dimensional surface temperature of roads, squares, and rooftops, while in situ NSAT usually collects urban canopy temperature at a certain height (e.g., 2 m) from the ground. Although satellite-based LST and in situ NSAT are not the same (Venter et al. 2021), satellite-based LST can overcome the underrepresentation of in situ NSAT measurements, especially in underdeveloped cities (Janatian et al. 2017;

Chakraborty et al. 2019; Verdin et al. 2020), and have great potential for identifying the world's hottest and coldest cities (Ho et al. 2014; Yoo et al. 2018). Satellite-based LST has been used as a proxy for NSAT to investigate the hottest and coldest spots over global land (Mildrexler et al. 2011; Scambos et al. 2018; Y. Zhao et al. 2021). However, previously identified spots are not in urban settlements but in sparsely or not populated areas. Pixel-by-pixel NSAT images derived from satellite LST data have been widely used to investigate the urban thermal environment (Ho et al. 2014; dos Santos 2020). However, satellite-derived NSAT has mostly been estimated at a relatively limited spatiotemporal scale, and the associated approaches used for NSAT mapping are mostly applicable at local or regional scales. Significant progress has been made in NSAT mapping over global lands using satellite-derived LST at a spatial resolution of 0.05° (Hooker et al. 2018; Verdin et al. 2020). Nevertheless, the used global in situ NSAT measurements have not been carefully screened to better suit NSAT mapping over urban landscapes and the NSAT products at 0.05° may be too coarse to resolve small- and medium-sized cities. Furthermore, although human thermal discomfort is closely related to both NSAT and relative humidity (Schoen 2005), most previous global urban temperature reports ignored the role of humidity in human discomfort (Chakraborty et al. 2022). Therefore, the ranking of the world's hottest and coldest cities, particularly from the perspective of human discomfort, has been difficult and highly uncertain.

Facing these challenges, it is crucial to design models for estimating NSAT at a fine scale by incorporating urban stations and extensive physical urban variables. Machine learning techniques can potentially characterize the complex and nonlinear relationships between in situ NSAT and various urban parameters (dos Santos 2020; Ho et al. 2014; Yoo et al. 2018). They provide an efficient and powerful means to map the urban NSAT and thermal discomfort index and consequently to examine the world's hottest and coldest cities and their geographical patterns. Therefore, here we combined carefully screened in situ measurements, various satellite-derived products, and the random forest model, and estimated both the monthly mean maximum and minimum NSATs and thermal discomfort index (termed TDI_{\max} and TDI_{\min}) over 13,135 cities worldwide from 2003 to 2019 at a 1-km resolution (refer to the "Strategies used for identifying the world's hottest and coldest cities" section). Moreover, the estimated urban TDI_{\max} and TDI_{\min} were then used to provide a ranking of the world's hottest and coldest cities. This study deepens the understanding of the urban population's exposure to extreme climates.

Input data

Urban boundary data. Standardized urban clusters are crucial for the ranking of the hottest and coldest cities. In this study, the urban cluster data were obtained from the Urban Centre Database of Global Human Settlement Layer (GHSL) (<https://ghsl.jrc.ec.europa.eu/index.php>). The GHSL dataset complies with the United Nations guidelines and it has been widely used in urban studies and statistical reports worldwide (European Commission 2020; Crippa et al. 2021; Tuholske et al. 2021). The GHSL built-up product was generated using automatic supervised classification with Landsat and Sentinel images. Its spatial resolution is 1 km and data of four years were produced (1975, 1990, 2000, and 2015). The GHSL dataset has a unified definition for urban areas and their surroundings. This study mainly focused on urban built-up area where the population size and urban area meet the definition of urban (Dijkstra et al. 2020). Due to this filter, rural settlements such as the renowned coldest town Oymyakon (Darack 2013) were filtered out. We finally identified 13,135 cities using the GHSL built-up product and the urban definition. The GHSL dataset classifies global cities into two categories according to income, i.e., high-income (HIC) and relatively low-income cities, with the latter being further grouped into three subclasses including upper- and middle-income (UMIC), lower- and middle-income (LMIC), and low-income (LIC) cities.

In situ NSAT data. High-quality in situ NSAT measurements are the basis for mapping NSAT over global cities. We employed in situ NSAT measurements from the Berkeley Earth dataset to train and validate the machine learning model. The Berkeley Earth dataset provides standardized NSAT measurements worldwide and it has been widely used for global climate research (<http://berkeleyearth.org>). The Berkeley dataset includes standardized monthly mean maximum and minimum NSATs over 47,031 stations worldwide during the period of 2003–19. Most of the stations from the Berkeley dataset are distributed over rural surfaces and are inappropriate for NSAT mapping over global urban landscapes (Fig. S2A). We therefore filtered the rural stations and only kept the stations directly in urban clusters or within a 15-km buffer zone of the urban boundary. By this filtering procedure, we finally obtained 10,127 urban (or quasi-urban) stations that would be used for global urban NSAT mapping (refer to Fig. S2D and Table S1).

MODIS data. We employed the *Aqua* MODIS LST product (MYD11A1, <https://lpdaac.usgs.gov/products/myd11a1v006/>, 2003–19, Collection 6) as one of the most crucial variables for mapping NSAT. We used MODIS LSTs from *Aqua* rather than *Terra* because the two overpasses of *Aqua* (i.e., ~0130 and ~1330 local solar time) correspond better to the daily maximum and minimum LSTs (Mildrexler et al. 2011; Y. Zhao et al. 2021). This dataset includes LST images across global land and has a spatial resolution of 1 km. The product has a relatively high accuracy with overall biases < 1.0 K under various land-cover types and atmospheric conditions (Wan et al. 2015). Although the MODIS LST product does have uncertainties (note S2), its robustness and quality have been well demonstrated for identifying the world’s hottest or coldest spots (Mildrexler et al. 2011; Y. Zhao et al. 2021). We also incorporated the monthly mean surface reflectance of MODIS in the red and near-infrared spectra with the spatial resolution of 500 m (<https://doi.org/10.5067/MODIS/MYD09A1.006>), as well as the 16-day MODIS enhanced vegetation index (EVI) data with the spatial resolution of 250 m (<https://doi.org/10.5067/MODIS/MYD13Q1.006>) to support the urban NSAT mapping.

Fine-resolution intracity data. Digital surface model (DSM) and human activity (e.g., population counts, impervious surface percentage, nighttime light, and urban texture) data are essential for the intracity NSAT mapping (Janatian et al. 2017; Yoo et al. 2018; dos Santos 2020). The 30-m resolution DSM data and the DSM-derived slope, latitude, and longitude were obtained from www.eorc.jaxa.jp/ALOS/en/dataset/aw3d30. Population data with the spatial resolution of 90 m were obtained from www.worldpop.org. Impervious surface percentage data with the spatial resolution of 90 m were obtained from <http://data.ess.tsinghua.edu.cn>. Nighttime light data with the spatial resolution of 1 km were obtained from <https://figshare.com>. Finally, urban texture parameters, including the dissimilarity and homogeneity of both ISP and MODIS EVI, were calculated from the grayscale co-occurrence matrix at the spatial resolution of 1 km. These texture parameters have been frequently used to represent the urban landscape (Puissant et al. 2005; Zhang et al. 2014).

Reanalysis data. We also employed reanalysis data to assist the urban NSAT mapping (Janatian et al. 2017; Yoo et al. 2018; dos Santos 2020). The ERA5-Land monthly averaged reanalysis dataset (<https://cds.climate.copernicus.eu/cdsapp#!/home>) was used in this study due to its relatively high spatial resolution (around 9 km). We retrieved three surface and atmospheric variables from the reanalysis data, including the 2-m air temperature, downward surface solar radiation, and downward surface thermal radiation (refer to Table S2). These variables were resampled to 1 km to match the MODIS LST data using the bicubic method.

Strategies used for identifying the world's hottest and coldest cities

Using the above datasets, we first estimated the monthly mean maximum and minimum 1-km NSATs and thermal discomfort index for global urban settlements during the period of 2003–19, and then provided a preliminary ranking of the world's hottest and coldest cities. Note that the global estimation of NSAT and thermal discomfort index may bias the accuracy of extreme values and then affect the ranking of the hottest and coldest cities (Hengl et al. 2018). We therefore estimated the NSAT and thermal discomfort index once again, but this time only using the datasets in the top 20% extreme cities identified by the first step. The overall framework used for identifying the world's hottest and coldest cities is provided in Fig. 1.

Step 1: Generation of monthly mean 1-km NSAT maps for global urban settlements. We used the random forest (RF; see the detailed model in Fig. S3) algorithm to obtain the complex

nonlinear relationships between the approximately 2.0 million in situ NSAT measurements (Table S3) and the associated input variables or features (i.e., the MODIS LST and auxiliary variables). With the obtained nonlinear relationships, we further estimated the monthly mean maximum and minimum NSATs for global urban settlements at the spatial resolution of 1 km during the period of 2003–19. In detail, we selected 18 features that are frequently used for NSAT mapping (Table S2). We divided the NSAT measurements into two categories, with 80% and 20% of the samples used for training and validation, respectively (refer to Table S1 for monthly samples). We then trained a RF model for each month, acquiring 12 daytime (for monthly mean maximum NSAT) and 12 nighttime models (for monthly mean minimum NSAT). To avoid the overfitting or underfitting problem, we assessed the relationship between the number of trees the RF model through the Akaike information criterion (AIC; Akaike 1998), Bayesian information criterion (BIC; Schwarz 1978), and out-of-bag error rate (O'Connell et al. 2015; Vuolo et al. 2018) based on the training sample pool. Our analysis indicates that

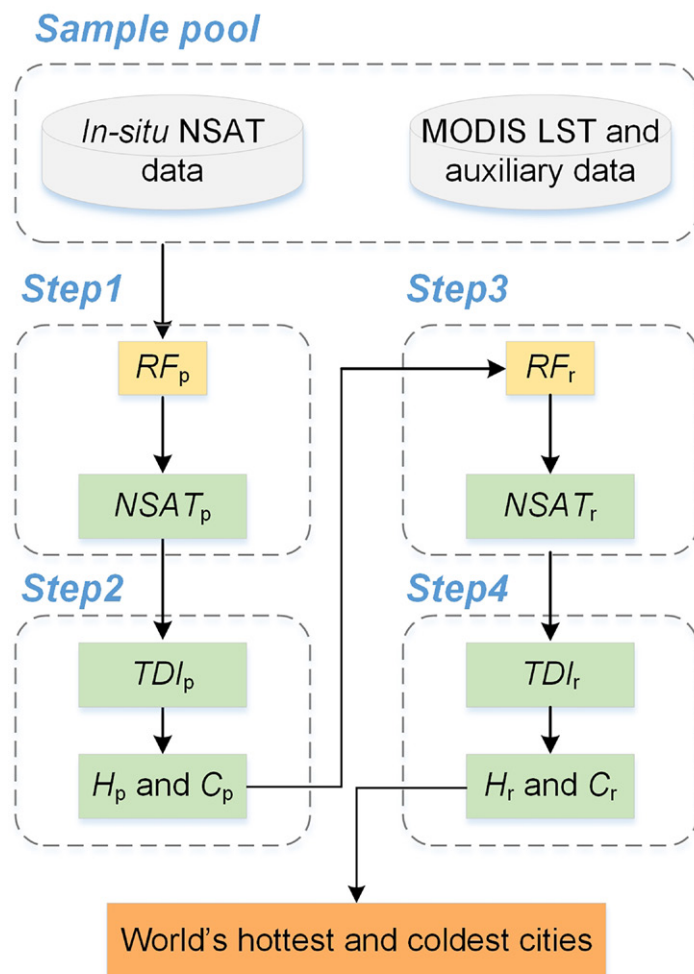


Fig. 1. A flowchart used to identify the world's hottest and coldest cities from thermal discomfort perspective. RF_p , $NSAT_p$, TDI_p , H_p , and C_p denote the random forest (RF) model (RF_p), monthly mean maximum and minimum NSATs ($NSAT_p$), monthly mean maximum and minimum thermal discomfort index (TDI_p), and ranking of hottest cities (H_p) and coldest cities (C_p) for global urban settlements modeled at the preliminary step; RF_r , $NSAT_r$, TDI_r , H_r , and C_r denote the refined RF model (RF_r), monthly mean maximum and minimum NSATs ($NSAT_r$), monthly mean maximum and minimum thermal discomfort index (TDI_r), and ranking of hottest cities (H_r) and coldest cities (C_r) based only on the top 20% hottest and coldest cities obtain in the preliminary step.

the performance of the three parameters for the RF model remains relatively stable for each month once the tree number exceeds 50 (Fig. S4). The validation demonstrates that the root-mean-squared error (RMSE) of the estimated monthly mean maximum NSAT ranges from 1.00° to 1.18°C while the associated mean absolute error (MAE) ranges from 0.72° to 0.85°C (Fig. S5). The RMSE and MAE for the monthly mean minimum NSAT are 0.93°–1.27°C and 0.68°–0.92°C, respectively (Fig. S6). In addition, we estimated the RMSE and MAE of the RF model for the cities with different income levels (note S3) and typical regions (note S4), the intra-urban variability of $NSAT_{max}$ and $NSAT_{min}$ in nine chosen cities with relatively dense weather stations (note S5), and the relative importance of the features (notes S4 and S6). These accuracies are generally on par with or better than those of previous studies (Ho et al. 2014; Yoo et al. 2018; dos Santos 2020). We finally estimated the monthly mean 1-km mean maximum and minimum NSATs for all the 13,135 urban settlements.

Step 2: Calculation of thermal discomfort index and preliminary ranking of the world's hottest and coldest cities for global urban settlements. We calculated the thermal discomfort index (TDI) proposed by Schoen (2005) to provide more physiologically relevant identification of climate extremes (note S7). The TDI incorporates both NSAT and humidity information and has been commonly used for estimating human perceived temperature (Lu and Kueppers 2015; Zhu et al. 2019). The TDI improves the suitability of traditional heat indices in low temperature ranges and overcomes the deficiency of wind chill indices in high temperature ranges (Schoen 2005). The TDI is more capable of model extrapolation when compared with the National Weather Service model (Schoen 2005). The TDI was calculated by the following formula (Schoen 2005):

$$TDI = T_{air} - 1.0799 \exp(0.03755T_{air}) \left[1 - \exp(0.0801T_{dew} - 1.1214) \right], \quad (1)$$

where T_{air} denotes the monthly NSAT and T_{dew} is the 2-m dewpoint temperature, both in degrees Celsius.

We followed the following steps to calculate TDI_{max} and TDI_{min} of each city and provided a preliminary ranking of the world's hottest and coldest cities for global urban settlements. 1) Using Eq. (1), we calculated the pixel-by-pixel 1-km monthly mean maximum and minimum TDI (termed TDI_{max} and TDI_{min}) with the estimated NSAT as well as resampled T_{dew} of 1 km spatial resolution retrieved from reanalysis data (note S8). 2) We calculated the maximum monthly TDI_{max} and minimum monthly TDI_{min} for each pixel within urban boundaries from 2003 to 2019. 3) We quantified the maximum monthly mean TDI_{max} and minimum monthly mean TDI_{min} for each city by averaging all the TDI values within each urban boundary. 4) We provided a preliminary ranking of the hottest and coldest cities (>10 km²) across global 13,135 settlements based on the average TDI_{max} and TDI_{min} .

Step 3: Recalculation of NSAT with the datasets only derived from the top 20% hottest and coldest cities in preliminary ranking. The global estimation of NSAT may distort the ranking of cities with extreme temperatures (Hengl et al. 2018). To improve the RF modeling of extreme temperatures, we therefore recalculated the NSAT only based on the datasets from the top 20% hottest and coldest cities in the preliminary ranking. More specifically, we reselected the datasets only within the masks of the top 20% cities used for refined RF modeling (Table S4). The estimation of NSAT was conducted using the same methodology as in the preliminary ranking. The validations show that the RMSE of the monthly mean maximum NSAT obtained with the refined RF modeling ranges from 0.80° to 1.05°C and the associated MAE ranges from 0.58° to 0.73°C (Fig. S7), while the RMSE of the monthly mean minimum NSAT ranges from 0.87° to 1.33°C and the associated MAE ranges from

0.64° to 0.99°C (Fig. S8). We finally updated the monthly mean maximum and minimum 1-km NSATs for the top 20% hottest and coldest cities.

Step 4: Identification of the world's hottest and coldest cities. Based on the refined NSAT only with the datasets from the top 20% cities with extreme temperatures, we recalculated the associated TDI through Eq. (1). We then calculated the associated TDI_{max} and TDI_{min} again for the top 20% cities and provided a refined ranking of the world's hottest and coldest cities.

Results and discussion

Satellite mapping of $NSAT_{max}$ and $NSAT_{min}$ across global cities. We collected approximately 2.0 million in situ NSAT measurements (Table S3) and chose 18 features (e.g., satellite-derived LST; Table S2) to map the monthly 1-km maximum and minimum NSAT (termed $NSAT_{max}$ and $NSAT_{min}$) for global settlements from 2003 to 2019. The random forest (RF) algorithm was used to obtain the complex nonlinear relationships between the NSAT measurements and these 18 features (refer to the “Strategies used for identifying the world's hottest and coldest cities” section). The global validation assessments showed that the RMSE and MAE for $NSAT_{max}$ were 1.10° and 0.78°C, respectively (Fig. 2b), whereas those for $NSAT_{min}$ were 1.10° and 0.79°C, respectively (Fig. 2f). Further verification confirmed that these accuracies were robust across the months (Figs. S5 and S6). These accuracies are on par with those of previous NSAT mapping studies at local scales (Ho et al. 2014; Yoo et al. 2018; dos Santos 2020). The monthly 1-km NSAT dataset covers every single patch of global urban settlements (Figs. 2a,e; see more global NSAT snapshots in Fig. S9), including low-income cities where urban stations are usually unavailable (e.g., small- and medium-sized urban clusters in Africa, India, Brazil, and China; Figs. 2c,d,g,h). This dataset includes small- and medium-sized cities, which may have significantly higher or lower temperatures than large cities equipped with weather stations. Therefore, this dataset enables a more objective ranking of the world's hottest and coldest cities.

Satellite-based ranking of city temperatures from human discomfort perspective. The thermal discomfort of urban residents is related to both NSAT and humidity (Schoen 2005). The monthly maximum and minimum thermal discomfort indices (TDI_{max} and TDI_{min}) over global urban settlements were calculated using the monthly $NSAT_{max}$ and $NSAT_{min}$ datasets (refer to the “Strategies used for identifying the world's hottest and coldest cities” section). The results for the two coastal cities of Shanghai and Cape Town, which have relatively high humidity, demonstrated that the calculated TDI_{max} can be more than 5.0°C higher than $NSAT_{max}$ and TDI_{min} can be 0.5°C lower than $NSAT_{min}$ (Fig. S10).

The results show that cities with high TDI_{max} are mostly located in South Asia, western Asia, northern Africa, and the western regions of North America (Fig. 3a). The top 10 hottest cities are primarily located in western Asia and South Asia, such as Bahrain, Qatar, Saudi Arabia, and Pakistan (Figs. 3b,e,g). The TDI_{max} for all these cities exceeds 46.3°C (Table S5), a value significantly greater than the alert threshold (40.6°C) for severe heat-related disorders (National Weather Service 2022). Manama (Fig. S11), Bahrain, which is located in an arid region, is the hottest city in the world, with the TDI_{max} reaching $48.18^\circ \pm 1.31^\circ\text{C}$ (Figs. 3,b,e,g). This temperature (48.18°C) is relatively lower than the previously identified hottest NSAT (56.7°C), which was recorded in unpopulated areas (El Fadli et al. 2013). However, this value was not recorded during a single occasional extreme event and reflects the mean thermal status of a populous city throughout an entire month. Manama, which is characterized by a subtropical high pressure climate, lies on an island in the Persian Gulf, and its urban landscapes are dominated by xerophytic shrubs (Fig. 3g and Fig. S11). Due to seawater evaporation, coastal Manama has 3–5 times higher relative humidity than Riyadh in the central Arabian Peninsula during hot

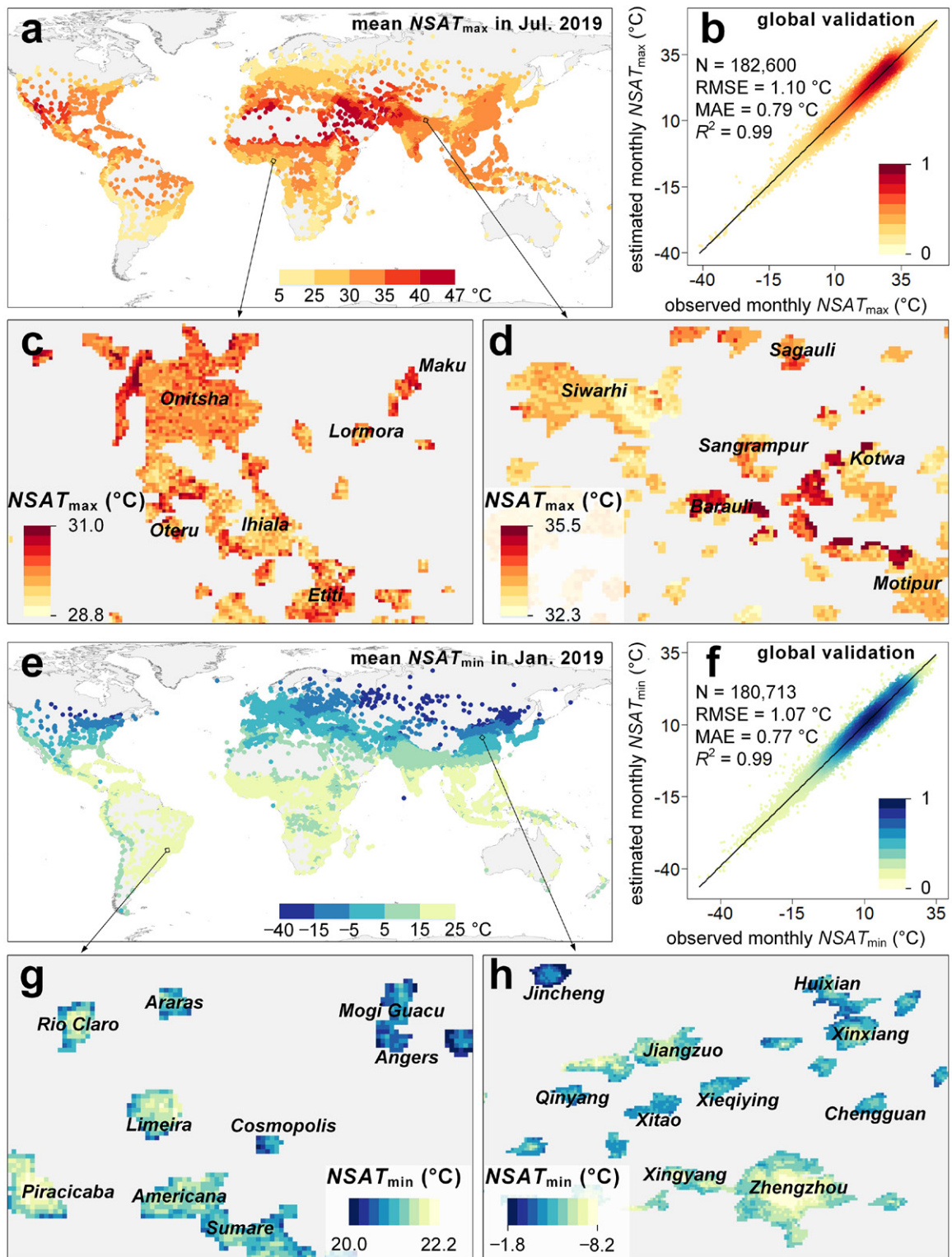


Fig. 2. Satellite-derived NSAT_{max} and NSAT_{min} maps and associated accuracy assessments for global urban settlements. (a) Mean NSAT_{max} in July 2019 for each city and (b) global validation of NSAT_{max}; 1-km spatial resolution NSAT_{max} in July 2019 for several typical small- and medium-sized urban clusters without available urban stations in (c) Africa and (d) India; (e) mean NSAT_{min} in January 2019 for each city and (f) global validation of NSAT_{min}; and 1-km spatial resolution NSAT_{min} in January 2019 for several typical small- and medium-sized urban clusters without available urban stations in (g) Brazil and (h) China.

months (Fig. S12). The local extreme NSAT, less effective cooling efficiency of urban shrubs, and excessive water vapor contributed to the extremely high TDI_{max} in Manama. Moreover, Manama is a relatively populous city with 1.25 million residents in the main urban areas (around 345 km²) of the city, indicating a large urban population exposed to extreme heat (Fig. S11).

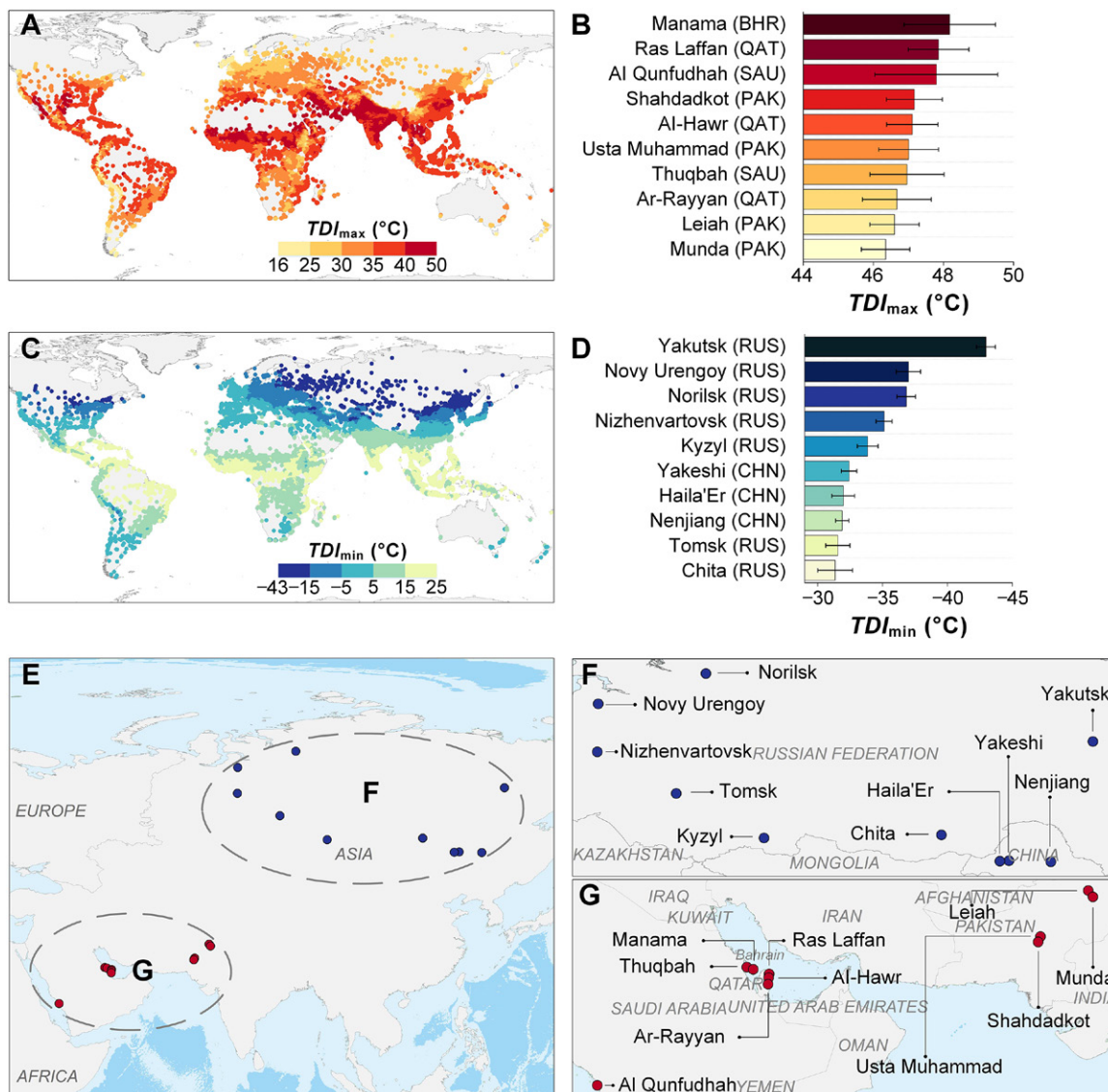


Fig. 3. Spatial distribution of satellite-derived TDI_{max} and TDI_{min} across global cities and the top 10 hottest and coldest cities. (a) TDI_{max} and (b) the top 10 hottest cities; (c) TDI_{min} and (d) the top 10 coldest cities; (e) spatial distribution of the top 10 hottest and coldest cities and zooming in on the (g) hottest and (f) coldest cities. BHR, QAT, SAU, PAK, RUS, and CHN denote Bahrain, Qatar, Saudi Arabia, Russia, and China, respectively.

In contrast, the cities with low TDI_{max} were mainly located in the northern regions of East Asia, North Asia, central Asia, eastern Europe, and North America (Fig. 3c). The top 10 coldest cities are located within the snow and semiarid regions of Russia and China (Figs. 3d,f), with the TDI_{min} value below -31.3°C (Table S6). These cities are characterized by a remarkable continental climate, and their TDI_{min} is extremely low because of the Siberian high during the winter. Yakutsk (Fig. S11), Russia, is the coldest city in the world, with a TDI_{min} of $-42.96^{\circ} \pm 0.72^{\circ}\text{C}$ (Fig. 3h). This observation is consistent with the previously acknowledged world's coldest city based on in situ NSATs (Phelan 2022) (www.pogodaiklimat.ru/climate/24959.htm). Moreover, this temperature ($-42.96^{\circ} \pm 0.72^{\circ}\text{C}$) is relatively lower than that previously recorded for a single extreme event (-64.4°C) because monthly values were used in this study. In addition, it was observed that the urban population of Yakutsk has increased by 17% in the last four decades, indicating enhanced urban population exposure to the extreme cold of this city.

Compared to the trend of cities in the bottom 80% (Fig. 4b), a smaller trend of cities in the upper 20% means that the extreme TDI_{max} or TDI_{min} variation is relatively small in about

20% of the world's cities, and thus, these cities face a greater threat from extreme heat or cold (Figs. 4e,f). More importantly, both TDI_{max} and TDI_{min} followed a power law (or logarithmic pattern) across global cities (Fig. 4a). The smaller overall trend of TDI_{max} (-0.11) than that of TDI_{min} (-0.38) suggests a relatively weaker temperature variation in TDI_{max} , implying that a relatively larger number of cities are threatened by extreme highs rather than extreme lows (Fig. 4a). In addition, most cities with extreme TDI_{max} or TDI_{min} have populations of less than 0.3 million (Figs. 4c,d), indicating that small- and medium-sized settlements dominate cities with extreme TDI_{max} or TDI_{min} . The cities with less than 0.3 million urban residents account for 81% of all the cities with extreme TDI_{max} (e.g., Yuma, Arizona, in the United States) and 83% of cities with extreme TDI_{min} (e.g., Aalborg in Denmark). In contrast, most cities with a large population, such as Guangzhou, Cairo, Chicago, and London for TDI_{max} , and Lyon, Cape Town, Miami, and Jakarta for TDI_{min} , are mainly characterized by relatively moderate TDI_{max} and TDI_{min} (Fig. 4a).

Implications

The results demonstrate that extreme temperatures are unevenly distributed across cities with different income levels. For example, extreme TDI_{max} and TDI_{min} are mainly distributed over cities in low-income regions (Fig. S13), such as north Africa, eastern Europe, and Asia, rather than in high-income regions (Figs. 3a,c). Although lower- and middle-income cities only account for 42% of all the cities considered, they constitute 81% of the top 20% of hottest cities. In these cities, higher urban population exposure and relatively poorer adaptation capability (such as a lack of air conditioning and cooling centers) significantly exacerbate the impacts of temperature extremes (Tuholske et al. 2021; L. K. Zhao et al. 2021) (Fig. 5).

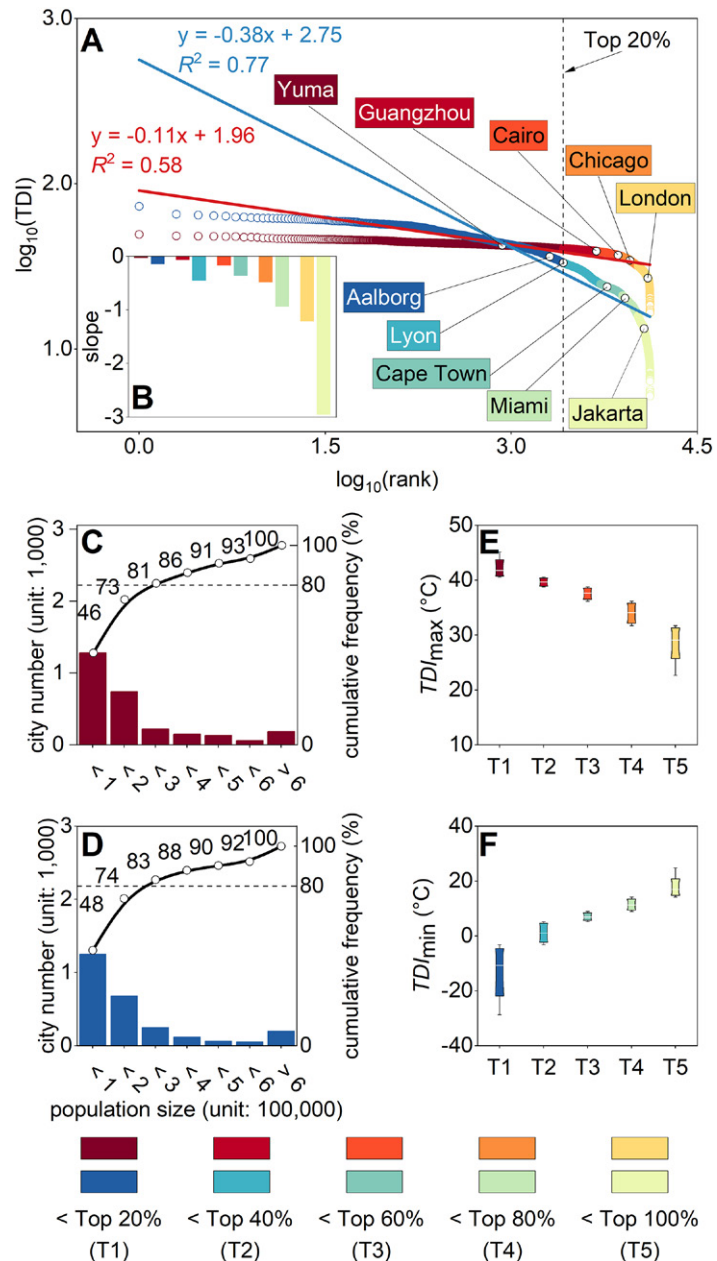


Fig. 4. Logarithmic variations of the satellite-derived thermal discomfort index (TDI) as a function of the ranking of global cities. (a) Logarithmic variations of TDI_{max} and TDI_{min} and 10 typical cities with extreme temperatures. In (a), the TDI_{min} has been inverted and offset by 30.0°C (giving $TDI_{min} > 0$) to ensure a meaningful logarithmic operation for all the TDI_{min} values. (b) The trends for different ranking percentiles, the number of cities with different population sizes for the top 20% (c) hottest and (d) coldest cities, and the TDI distribution for ranking percentiles of (e) hottest and (f) coldest cities.



Fig. 5. Proportions of the global cities and the top 20% hottest (or coldest) cities at different income levels.

Similarly, although upper- and middle-income cities account for 38% of the cities, they constitute 61% of the top 20% of the coldest cities (Fig. 5). The latest projections show that 90% of the world's new urban population will occur in regions with relatively low economic development levels by 2050 (United Nations 2019). However, the lack of climate adaptation infrastructure in these regions will considerably increase the risk of the urban population under future climate change (Eckstein et al. 2019). This risk to disadvantaged communities is even more concerning because of intraurban disparities in heat exposure (Chakraborty et al. 2019). As we prepare for a warmer planet, local urban planners in underdeveloped cities should be aware of the significance of climate-resilient infrastructure in the design of adaptation strategies.

These results indicate that most of the top 20% of the hottest and coldest cities are small or medium sized, necessitating the importance of improving climate change adaptation strategies for risk mitigation in these cities (Fig. 4). Lower- and middle-income cities accounted for 82% and upper- and middle-income cities accounted for 59% of the small- or medium-sized cities with extremely high and low temperatures, respectively (Fig. S14). However, small- and medium-sized cities have been excluded from urban extreme climate adaptation studies for a long time (Watts 2017), and they have lower levels of climate awareness than large cities (Reckien et al. 2018). Therefore, to enhance the awareness of climate extremes for small- and medium-sized cities, policy-makers should develop more targeted approaches, such as disseminating more rankings of the world's hottest and coldest cities in newspapers or magazines (Lee et al. 2015; Luís et al. 2018). The current study provides more evidence of the increased risk of temperature extremes in small- and medium-sized cities. To reduce the risks of global climate change for larger and generally more vulnerable populations, adaptation strategies should be developed specifically for these small- and medium-sized cities.

Acknowledgments. We gratefully acknowledge the National Natural Science Foundation of China (42171306) for providing the funding to support this study. We also thank the support from the National Youth Talent Support Program of China, China Scholarship Council (CSC), and Program-B for Outstanding Ph.D. candidate of Nanjing University (202201B039). T. C.'s contribution was supported by COMPASS-GLM, a multi-institutional project supported by the U.S. Department of Energy, Office of Science, Office of Biological and Environmental Research as part of the Earth and Environmental Systems Modeling program. PNNL is operated for the Department of Energy by Battelle Memorial

Institute under Contract DE-AC05-76RL01830. W. Z. conceived and designed the study; J. L. performed the data analysis; J. L. and W. Z. wrote the paper; and T. C., Z. L., H. D., W. L., M. L., L. L., S. M., H. F., S. W., F. H., and M. L. contributed insights in modeling, results, and discussions. The authors declare no competing interests.

Data availability statement. All input data for global estimation of monthly mean maximum and minimum 1-km near-surface temperature (NSAT) and thermal discomfort index are publicly available: urban boundary data (<https://ghsl.jrc.ec.europa.eu/index.php>), in situ near-surface temperature (NSAT) data (<http://berkeleyearth.org/>), *Aqua* MODIS LST product (MYD11A1, <https://lpdaac.usgs.gov/products/myd11a1v006/>, 2003–19, Collection 6), monthly mean surface reflectance of MODIS in the red and near-infrared spectra (<https://doi.org/10.5067/MODIS/MYD09A1.006>), 16-day MODIS enhanced vegetation index (EVI) data (<https://doi.org/10.5067/MODIS/MYD13Q1.006>), 30-m resolution DSM data and the DSM-derived slope, latitude, and longitude (www.eorc.jaxa.jp/ALOS/en/dataset/aw3d30), population data (www.worldpop.org), impervious surface percentage data (<http://data.ess.tsinghua.edu.cn>), and nighttime lighting data (<https://figshare.com>). All computer code used in the data analysis is available from the corresponding author upon reasonable request.

References

- Akaike, H., 1998: Information theory and an extension of the maximum likelihood principle. *Selected Papers of Hirotugu Akaike*, E. Parzen, K. Tanabe, and G. Kitagawa, Eds., Springer Series in Statistics, Springer, 199–213, https://link.springer.com/chapter/10.1007/978-1-4612-1694-0_15.
- Amos, J., 2013: Coldest spot on Earth identified by satellite. BBC News, accessed 28 September 2022, www.bbc.com/news/science-environment-25287806.
- Azarderakhsh, M., S. Prakash, Y. Zhao, and A. AghaKouchak, 2020: Satellite-based analysis of extreme land surface temperatures and diurnal variability across the hottest place on Earth. *IEEE Geosci. Remote Sens. Lett.*, **17**, 2025–2029, <https://doi.org/10.1109/LGRS.2019.2962055>.
- BBC News, 2010: How do you survive in the coldest place on Earth? BBC News, accessed 28 September 2022, www.bbc.com/news/world-11875131.
- , 2017: Growing up in -60°C . BBC News, accessed 28 September 2022, www.bbc.com/news/in-pictures-41914876.
- , 2020: 'Highest temperature on Earth' as Death Valley, US hits 54.4°C . BBC News, accessed 28 September 2022, www.bbc.com/news/world-us-canada-53788018.
- Chakraborty, T., and X. Lee, 2019: A simplified urban-extent algorithm to characterize surface urban heat islands on a global scale and examine vegetation control on their spatiotemporal variability. *Int. J. Appl. Earth Obs. Geoinf.*, **74**, 269–280, <https://doi.org/10.1016/j.jag.2018.09.015>.
- , A. Hsu, D. Many, and G. Sheriff, 2019: Disproportionately higher exposure to urban heat in lower-income neighborhoods: A multi-city perspective. *Environ. Res. Lett.*, **14**, 105003, <https://doi.org/10.1088/1748-9326/ab3b99>.
- , Z. S. Venter, Y. Qian, and X. Lee, 2022: Lower urban humidity moderates outdoor heat stress. *AGU Adv.*, **3**, e2022AV000729, <https://doi.org/10.1029/2022AV000729>.
- Clemens, K. K., A. M. Ouédraogo, L. Li, J. A. Voogt, J. Gilliland, E. S. Kravynhoff, S. Leroyer, and S. Z. Shariff, 2021: Evaluating the association between extreme heat and mortality in urban southwestern Ontario using different temperature data sources. *Sci. Rep.*, **11**, 8153, <https://doi.org/10.1038/s41598-021-87203-0>.
- Crippa, M., and Coauthors, 2021: Global anthropogenic emissions in urban areas: Patterns, trends, and challenges. *Environ. Res. Lett.*, **16**, 074033, <https://doi.org/10.1088/1748-9326/ac00e2>.
- Darack, E., 2013: The 10 worst weather places in the world. *Weatherwise*, **66**, 12–19, <https://doi.org/10.1080/00431672.2013.839230>.
- de León, C., and J. Schwartz, 2020: Death Valley just recorded the hottest temperature on Earth. *New York Times*, 7 December, www.nytimes.com/2020/08/17/climate/death-valley-hottest-temperature-on-earth.html.
- Dijkstra, L., E. Hamilton, S. Lall, and S. Wahba, 2020: How do we define cities, towns, and rural areas? World Bank Blogs, accessed 28 January 2023, <https://blogs.worldbank.org/sustainablecities/how-do-we-define-cities-towns-and-rural-areas>.
- dos Santos, R. S., 2020: Estimating spatio-temporal air temperature in London (UK) using machine learning and Earth observation satellite data. *Int. J. Appl. Earth Obs. Geoinf.*, **88**, 102066, <https://doi.org/10.1016/j.jag.2020.102066>.
- Eckstein, D., V. Künzel, L. Schäfer, and M. Wings, 2019: Global Climate Risk Index 2020: Who suffers most from extreme weather events? Weather-related loss events in 2018 and 1999 to 2018. Germanwatch Rep., 44 pp., https://germanwatch.org/sites/default/files/20-2-01e%20Global%20Climate%20Risk%20Index%202020_15.pdf.
- El Fadli, K. I., and Coauthors, 2013: World Meteorological Organization assessment of the purported world record 58°C temperature extreme at El Azizia, Libya (13 September 1922). *Bull. Amer. Meteor. Soc.*, **94**, 199–204, <https://doi.org/10.1175/BAMS-D-12-00093.1>.
- European Commission, 2020: A recommendation on the method to delineate cities, urban and rural areas for international statistical comparisons. European Commission Rep., 33 pp., <https://unstats.un.org/unsd/statcom/51st-session/documents/BG-Item3j-Recommendation-E.pdf>.
- Farmer, B., 2021: Hotter than the human body can handle: Pakistan city broils in world's highest temperatures. *Telegraph*, 28 June, www.telegraph.co.uk/global-health/climate-and-people/hotter-human-body-can-handle-pakistan-city-broils-worlds-highest.
- Haddad, M., 2021: Mapping the hottest temperatures around the world. Al Jazeera, accessed 28 September 2022, www.aljazeera.com/news/2021/7/1/interactive-mapping-hottest-temperatures-around-world.
- Hengl, T., M. Nussbaum, M. N. Wright, G. B. Heuvelink, and B. Gräler, 2018: Random forest as a generic framework for predictive modeling of spatial and spatio-temporal variables. *PeerJ*, **6**, e5518, <https://doi.org/10.7717/peerj.5518>.
- Ho, H. C., A. Knudby, P. Sirovyak, Y. Xu, M. Hodul, and S. B. Henderson, 2014: Mapping maximum urban air temperature on hot summer days. *Remote Sens. Environ.*, **154**, 38–45, <https://doi.org/10.1016/j.rse.2014.08.012>.
- Hooker, J., G. Duveiller, and A. Cescatti, 2018: A global dataset of air temperature derived from satellite remote sensing and weather stations. *Sci. Data*, **5**, 180246, <https://doi.org/10.1038/sdata.2018.246>.
- Janatian, N., M. Sadeghi, S. H. Sanaeinejad, E. Bakhshian, A. Farid, S. M. Hashemina, and S. Ghazanfari, 2017: A statistical framework for estimating air temperature using MODIS land surface temperature data. *Int. J. Climatol.*, **37**, 1181–1194, <https://doi.org/10.1002/joc.4766>.
- Lee, T. M., E. M. Markowitz, P. D. Howe, C. Y. Ko, and A. A. Leiserowitz, 2015: Predictors of public climate change awareness and risk perception around the world. *Nat. Climate Change*, **5**, 1014–1020, <https://doi.org/10.1038/nclimate2728>.
- Lu, Y., and L. Kueppers, 2015: Increased heat waves with loss of irrigation in the United States. *Environ. Res. Lett.*, **10**, 064010, <https://doi.org/10.1088/1748-9326/10/6/064010>.
- Luis, S., C.-M. Vaclair, and M. L. Lima, 2018: Raising awareness of climate change causes? Cross-national evidence for the normalization of societal risk perception of climate change. *Environ. Sci. Policy*, **80**, 74–81, <https://doi.org/10.1016/j.envsci.2017.11.015>.
- Mildrexler, D. J., M. Zhao, and S. W. Running, 2011: Satellite finds highest land skin temperatures on Earth. *Bull. Amer. Meteor. Soc.*, **92**, 855–860, <https://doi.org/10.1175/2011BAMS3067.1>.
- Muller, C. L., L. Chapman, C. S. B. Grimmond, D. T. Young, and X. Cai, 2013: Sensors and the city: A review of urban meteorological networks. *Int. J. Climatol.*, **33**, 1585–1600, <https://doi.org/10.1002/joc.3678>.
- National Weather Service, 2022: Heat: A major killer. Accessed 28 September 2022, www.nws.noaa.gov/om/heat/index.shtml.
- O'Connell, J., U. Bradter, and T. G. Benton, 2015: Wide-area mapping of small-scale features in agricultural landscapes using airborne remote sensing. *ISPRS J. Photogramm. Remote Sens.*, **109**, 165–177, <https://doi.org/10.1016/j.isprsjprs.2015.09.007>.
- Phelan, J., 2022: What is the coldest city in the world? Livescience, accessed 28 September 2022, www.livescience.com/what-is-the-coldest-city.
- Puissant, A., J. Hirsch, and C. Weber, 2005: The utility of texture analysis to improve per-pixel classification for high to very high spatial resolution imagery. *Int. J. Remote Sens.*, **26**, 733–745, <https://doi.org/10.1080/01431160512331316838>.
- Readfearn, G., 2020: Death Valley temperature rises to 129.9°F —Possibly the hottest ever reliably recorded. *Guardian*, accessed 28 September 2022, www.theguardian.com/us-news/2020/aug/17/death-valley-temperature-rises-to-544c-possibly-the-hottest-ever-reliably-recorded.
- Reckien, D., and Coauthors, 2018: How are cities planning to respond to climate change? Assessment of local climate plans from 885 cities in the EU-28. *J. Cleaner Prod.*, **191**, 207–219, <https://doi.org/10.1016/j.jclepro.2018.03.220>.
- Samenow, J., 2016: New analysis shreds claim that Death Valley recorded Earth's highest temperature in 1913. *Washington Post*, 25 October, www.washingtonpost.com/news/capital-weather-gang/wp/2016/10/25/new-analysis-shreds-claim-that-death-valley-recorded-earths-hottest-temperature-in-1913.

- Scambos, T.A., G. G. Campbell, A. Pope, T. Haran, A. Muto, M. Lazzara, C. H. Reijmer, and M. R. van den Broeke, 2018: Ultralow surface temperatures in East Antarctica from satellite thermal infrared mapping: The coldest places on Earth. *Geophys. Res. Lett.*, **45**, 6124–6133, <https://doi.org/10.1029/2018GL078133>.
- Schoen, C., 2005: A new empirical model of the temperature–humidity index. *J. Appl. Meteor.*, **44**, 1413–1420, <https://doi.org/10.1175/JAM2285.1>.
- Schwarz, G., 1978: Estimating the dimension of a model. *Ann. Stat.*, **6**, 461–464.
- Tuholske, C., K. Caylor, C. Funk, A. Verdin, S. Sweeney, K. Grace, P. Peterson, and T. Evans, 2021: Global urban population exposure to extreme heat. *Proc. Natl. Acad. Sci. USA*, **118**, e2024792118, <https://doi.org/10.1073/pnas.2024792118>.
- Turner, J., and Coauthors, 2009: Record low surface air temperature at Vostok station, Antarctica. *J. Geophys. Res.*, **114**, D24102, <https://doi.org/10.1029/2009JD012104>.
- United Nations, 2019: World urbanization prospects: The 2018 revision, highlights. UN Department of Economic and Social Affairs Rep., 38 pp., <https://population.un.org/wup/Publications/Files/WUP2018-Highlights.pdf>.
- Venter, Z. S., T. Chakraborty, and X. Lee, 2021: Crowdsourced air temperatures contrast satellite measures of the urban heat island and its mechanisms. *Sci. Adv.*, **7**, eabb9569, <https://doi.org/10.1126/sciadv.abb9569>.
- Verdin, A., C. Funk, P. Peterson, M. Landsfeld, C. Tuholske, and K. Grace, 2020: Development and validation of the CHIRTS-daily quasi-global high-resolution daily temperature data set. *Sci. Data*, **7**, 303, <https://doi.org/10.1038/s41597-020-00643-7>.
- Vuolo, F., M. Neuwirth, M. Immitzer, C. Atzberger, and W. T. Ng, 2018: How much does multi-temporal Sentinel-2 data improve crop type classification? *Int. J. Appl. Earth Obs. Geoinf.*, **72**, 122–130, <https://doi.org/10.1016/j.jag.2018.06.007>.
- Wan, Z., S. Hook, and G. Hulley, 2015: MYD11A1 MODIS/Aqua land surface temperature/emissivity daily L3 global 1 km SIN grid V006. LP DAAC, accessed 28 September 2022, <https://doi.org/10.5067/MODIS/MYD11A1.006>.
- Watts, M., 2017: Cities spearhead climate action. *Nat. Climate Change*, **7**, 537–538, <https://doi.org/10.1038/nclimate3358>.
- World Economic Forum, 2019: The Global Risks Report 2019. World Economic Forum Rep., 114 pp., www3.weforum.org/docs/WEF_Global_Risks_Report_2019.pdf.
- Yoo, C., J. Im, S. Park, and L. J. Quackenbush, 2018: Estimation of daily maximum and minimum air temperatures in urban landscapes using MODIS time series satellite data. *ISPRS J. Photogramm. Remote Sens.*, **137**, 149–162, <https://doi.org/10.1016/j.isprsjprs.2018.01.018>.
- Zhang, Y., H. Zhang, and H. Lin, 2014: Improving the impervious surface estimation with combined use of optical and SAR remote sensing images. *Remote Sens. Environ.*, **141**, 155–167, <https://doi.org/10.1016/j.rse.2013.10.028>.
- Zhao, L. K., and Coauthors, 2021: Global multi-model projections of local urban climates. *Nat. Climate Change*, **11**, 152–157, <https://doi.org/10.1038/s41558-020-00958-8>.
- Zhao, Y., H. Norouzi, M. Azarderakhsh, and A. AghaKouchak, 2021: Global patterns of hottest, coldest, and extreme diurnal variability on Earth. *Bull. Amer. Meteor. Soc.*, **102**, E1672–E1681, <https://doi.org/10.1175/BAMS-D-20-0325.1>.
- Zhou, D., and Coauthors, 2019: Satellite remote sensing of surface urban heat islands: Progress, challenges, and perspectives. *Remote Sens.*, **11**, 48, <https://doi.org/10.3390/rs11010048>.
- Zhu, J., S. Wang, and G. Huang, 2019: Assessing climate change impacts on human-perceived temperature extremes and underlying uncertainties. *J. Geophys. Res. Atmos.*, **124**, 3800–3821, <https://doi.org/10.1029/2018JD029444>.